Oxidation of ferritic stainless steel interconnects: Thermodynamic and kinetic assessment

Voramon S. Dheeradhada, Hongbo Cao, Matthew J. Alinger*

GE Global Research, 1 Research Circle, Niskayuna, NY 12309, United States

ARTICLE INFO

ABSTRACT

Planar solid oxide fuel cells with yttria-stabilized zirconia electrolytes typically operate at temperatures in the range of 700–850 °C. The maximum temperature is limited by the use of ferritic stainless steel interconnects which offer significant advantages such as low cost and high thermal and electronic conductivity over traditional ceramic interconnects. However, these alloys rely on the formation of a protective chromia scale for oxidation resistance that results in an increase in ohmic resistance and can volatilize leading to a loss of cathode catalytic activity. To better understand the oxidation behavior of chromia forming ferritic stainless steels, thermodynamic modeling was performed in conjunction with experimental oxidation testing and empirical kinetic evaluation. The phase stability and oxidation behavior of the Fe–Cr–O ternary system were assessed using thermodynamic calculations. Calculated ternary phase diagrams were validated against the experimental oxidation data of Fe–20Cr and Fe–18Cr ferritic stainless steels, GE-13L and AL-441HP, respectively. Results indicate that the use of accelerated testing, such as exposing the system to higher temperatures, can lead to changes in phase equilibria and the oxidation kinetics of the alloys. Through combined thermodynamic assessment and controlled oxidation experiments, the oxidation behavior of high-chromium ferritic stainless steels is presented and discussed.

1. Introduction

Solid oxide fuel cells (SOFCs) are solid state energy conversion devices that operate by electrochemically converting fuel and oxidant gases into electricity without combustion. The reduction in SOFC operating temperature due to recent development in materials and fabrication techniques enable the use of ferritic stainless steels as interconnects for SOFCs [1,2]. Ferritic stainless steels offer many advantages over traditional ceramic interconnects, such as higher thermal and electronic conductivity, reasonable thermal expansion matching, relative ease of fabrication and decreased machining costs [3]. However, the formation of thermally grown chromium oxide on ferritic stainless steel alloys results in an increase in ohmic resistance and can lead to the loss of cathode catalytic activity (through Cr volatilization) known as cathode poisoning [4].

Oxidation behavior of ferritic stainless steels has been extensively studied. It has been found that oxide growth depends on many factors including alloy composition, oxygen partial pressure, temperature, and exposure time [5–8]. The effect of alloy com-

position on the oxidation behavior of engineering alloys can be complex, in particular when dealing with minor alloying and impurity elements. As such, the current study primarily investigates the effects of major alloying elements, specifically Cr and Fe, on the oxidation behavior.

When exposed to air or oxygen at 800–1000 °C, ferritic stainless steels form chromium oxide, $(Fe,Cr,Mn)_3O_4$-Spinel, iron oxides, and/or their combinations such as iron–chromium oxides. Kubaschewski and Hopkins [9] proposed that the rate of the early oxidation of iron–chromium alloy is rapid due to the formation of iron oxide. During the initial oxidation stages, iron-rich Corundum oxide $(Fe_2O_3–Cr_2O_3)$ forms, subsequently converting to chromium-rich oxide with time [8]. SOFC performance is strongly influenced by the electrical resistance of the stainless steel interconnect. Therefore, increased cell resistance as a result of the oxide scale is a direct consequence. Hence, it is important to identify phase stability, material responses under the oxidation conditions, and the oxidation kinetics of stainless steel interconnects at operating temperatures (700–850 °C). Given anticipated lifetimes of 40,000 h, accelerated testing is desirable. However, accelerated testing at elevated temperatures may influence phase equilibria and oxidation mechanism and kinetics of the system to the point where high temperature data is no longer relevant to actual operating temperatures. A systematic understanding of oxidation

* Corresponding author. Tel.: +1 518 387 5124; fax: +1 518 387 5576.
E-mail address: alinger@ge.com (M.J. Alinger).

behavior and oxidation kinetics of ferritic stainless steel interconnects as a function of temperature will enable the prediction of the long term effects of chromium oxide that forms as a result of exposure to SOFC cathode operating conditions.

The aim of this work is to assess the oxidation behavior of ferritic stainless steels using thermodynamic modeling and experimentally derived kinetics. Two ferritic steels were selected for this study: GE-13L and AL-441HP. GE-13L is an alloy developed by GE for SOFC interconnect applications. AL-441HP is a commercial chromia-forming stainless steel available from Allegheny Ludlum which is a lower cost alternative. Thermodynamic modeling will be presented in terms of isothermal sections, stability diagrams, as well as calculated phase fraction diagrams. Oxidation behavior of the two steels will be discussed in term of kinetics assessment over the temperature range of 800–1000 °C.

2. Methodology

2.1. Thermodynamic modeling

A consistent thermodynamic description of Fe–Cr–O ternary was obtained based on the published thermodynamic modeling of the quaternary Fe–Cr–Ni–O system [15]. All of the solid phases were modeled by the Compound Energy Formalism (CEF) [16], which has been widely used to describe phases using two or more sublattices in CALPHAD assessments. The molar Gibbs energy of a phase consists of three terms as given below,

$$G_m^\varphi = {}^{ref}G_m^\varphi + {}^{id}G_m^\varphi + {}^{ex}G_m^\varphi \tag{1}$$

with the first term on the right hand side of Eq. (1) being the Gibbs energy in the reference state, the second term the ideal mixing term, and the third one the excess term, which may be determined through an optimization procedure. For this particular case, since all of the solid metallic phases and oxide phases undergo a magnetic transition, the magnetic contribution to the Gibbs energy was incorporated [17,21]. The magnetic contribution is described by Eq. (2).

$$^{mag}G = RT \ln(\beta + 1) f(\tau) \tag{2}$$

where $\tau = T/Tc$, Tc is the Curie (or Neel) temperature and β is the effective magnetic moment [17,21]. It is worth pointing out that in Ref. [15] one of the parameters for the Cr-rich Spinel phase was found to be in error, which causes the Cr_3O_4 phase to be artificially stable at low temperatures. A correction was made to fix this problem by adjust parameters for those end members with Cr^{2+} on the first sublattice.

In addition to a reliable thermodynamic description, robust software is essential for the successful application of the CALPHAD approach. In the present study, Pandat 8.0 [22] was used to perform the phase diagram calculations. The overall system pressure was kept at 1 atm for all calculations.

2.2. Alloy selection for oxidation testing

GE-13L is a chromia forming ferritic stainless steel developed by GE specifically for SOFC interconnect applications. It is an Fe–20 wt% Cr steel (Table 1) that was optimized for machinability, strength, and oxidation resistance at an SOFC operating temperature of ~800 °C. Given that silicon and aluminum impurities in SOFC interconnect alloys can lead to the formation of highly resistive oxide scales, the processing of this alloy was performed in vacuum to limit the inclusion of these detrimental elements.

Stainless steel 441 (AL-441HP) is a commercial ferritic stainless steel with 18 wt% chromium (Table 1). AL-441HP is readily available and does not require sophisticated alloy manufacturing methods

(such as vacuum processing) making it more cost effective. Therefore, AL-441HP is an attractive option as a lower cost option for SOFC interconnects.

The oxidation study of GE-13L and AL-441HP was aimed at understanding the oxidation behavior and kinetics of both stainless steels as a function of temperature in the range of 800–1000 °C, where 800 °C is the target SOFC operating temperature. However, accelerated testing through higher temperatures such as 900 or 1000 °C, must be well understood in order to evaluate the validity of such techniques.

The oxidation data will be used to identify any fundamental differences in oxidation behavior between the two steels. The focus of the current study will be to identify oxide phases formed, characterize oxidation behavior, and establish the parabolic rate constants. The resulting understanding will enable prediction of long-term degradation effects (in terms of oxide thicknesses) due to oxide scale formation for the two candidate materials.

2.3. Oxidation testing

The oxidation behavior of ferritic stainless steels GE-13L and AL-441HP was studied using cold-rolled sheet material. Samples of 25 mm × 25 mm × 0.5 mm or 25 mm × 12.5 mm × 0.5 mm were machined from each steel for oxidation tests.

Individual samples were ultrasonically cleaned, weighed, and physically measured prior to oxidation testing. Continuous isothermal oxidation tests were conducted at 800, 900, and 1000 °C in laboratory air up to 200 h. After testing, samples were removed from the furnace, air cooled and weighed at room temperature. Weight change was determined from the difference before and after the oxidation testing normalized by the sample surface area. The weight gain of the samples is indicative of oxygen ingress and formation of an oxide scale while weight loss indicates the loss of material through spallation and the loss via volatilization of oxides such as chromia.

The oxide scale surfaces were examined by X-ray diffraction, after which the oxidized samples were sectioned and polished to characterize the oxide scale in a cross-sectional orientation. The cross sections were analyzed by scanning electron microscopy (SEM) equipped with energy dispersive X-ray spectroscopy (EDS).

2.4. Kinetic analysis methodology

A kinetic model for each testing temperature was determined by Eq. (3) [10]. The kinetic parameter, n, signifies the kinetic model for the oxidation behavior of materials. For the ideal diffusion-controlled oxidation of pure metals, the oxidation kinetics should follow a parabolic rate law represented in Eq. (4) [24]. Using the weight change and the oxide thickness data, the kinetic parameter (n) and parabolic rates for samples oxidized at 800, 900, and 1000 °C were calculated and are presented and discussed in the following section.

Oxidation kinetic model calculation:

$$\frac{\Delta w}{Area} = kt^n \tag{3}$$

where Δw is the weight change, $Area$ is the surface area of the sample, k is a constant, t is the time, and n is the kinetic model parameter.

Parabolic rate law calculation:

$$W^2 = k_p t + C \tag{4}$$

where W is the weight change per unit area, k_p is a parabolic constant, and C is a constant.

Table 1
Chemistries of GE-13L and AL-441HP [18].

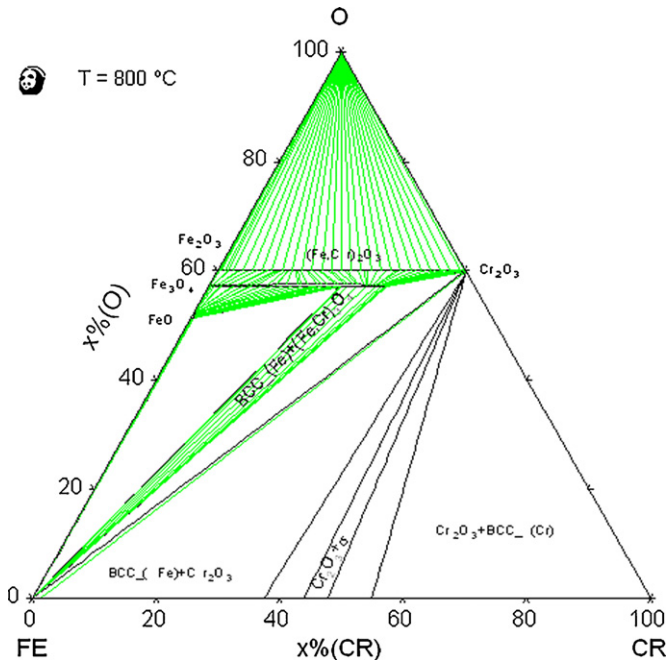| Alloys	Weight (%)							
	Fe	Cr	Ti	Nb	Si	Mn	W	Others
GE-13L	Bal.	20					4–5	RE
AL-441HP	Bal.	18	0.1–0.5	1.0 max	1.0 max	1.0 max		C, P, S

Note: RE is reactive element.

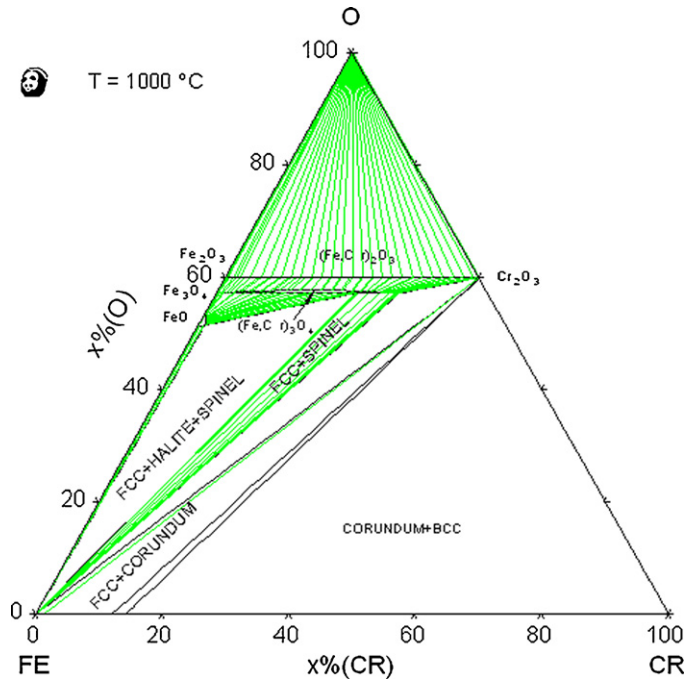**Fig. 1.** Calculated isothermal section of Fe–Cr–O at 800 °C.

Fig. 2. Calculated isothermal section of Fe–Cr–O at 1000 °C.

3. Results

3.1. Calculated ternary isothermal sections at 800 and 1000 °C

Fig. 1 shows a calculated phase diagram of the Fe–Cr–O system at 800 °C. In the present study, all calculations are based on atomic percent unless indicated otherwise. According to this isothermal section, the stable oxides are Corundum [(Fe,Cr)$_2$O$_3$], Fe-rich Spinel [(Fe,Cr)$_3$O$_4$], and Halite [FeO]. The Corundum phase forms a continuous solid solution between two binary compounds: Fe$_2$O$_3$ and Cr$_2$O$_3$. In addition, the oxygen concentration in Corundum is constant at 60 at.%. Given that Cr$_3$O$_4$ is not stable at this temperature, the FeCr$_2$O$_4$-Spinel phase extends from the binary Fe$_3$O$_4$ to FeCr$_2$O$_4$. There is a large two-phase field between BCC-(Fe) and the Cr-rich (Fe,Cr)$_3$O$_4$ Spinel phase, Cr$_2$O$_3$. This indicates that for a Fe-rich alloy, for example, Fe–20Cr, the BCC phase will be stable at this temperature and it should be in equilibrium directly with Cr$_2$O$_3$. The same applies for the Cr-rich corner.

Fig. 2 shows a calculated isothermal section at 1000 °C. The (O)-rich portion is almost identical to the diagram at 800 °C, except the oxygen solubility is slightly higher in the Spinel phase. For the Fe-rich region, Cr concentration below ∼12 at.% results in FCC-(Fe) phase whereas BCC-(Fe) is a stable phase in alloys with Cr concentration greater than 12 at.%. Moreover, since the temperature is above the critical point of the miscibility gap between BCC-(Fe) and BCC-(Cr) (binary phase diagram), the two BCC phases become undistinguishable. As a result, the two-phase field of BCC + Cr$_2$O$_3$ is significantly enlarged. In the current study, the isothermal section for 900 °C was also calculated. However, it is found that the phase

equilibrium relationship is very similar to that of 1000 °C as shown in Fig. 2. Therefore, it is not shown here.

3.2. Stability diagram (predominance, or chemical potential diagram)

Fig. 3 shows the calculated stability diagram at 800 °C. At PO$_2$ higher than 10^{-8}, Corundum is the most stable phase. Depending on the composition of the alloy, the Corundum phase could be either Fe-rich or Cr-rich. In the intermediate PO$_2$ regime, several oxides
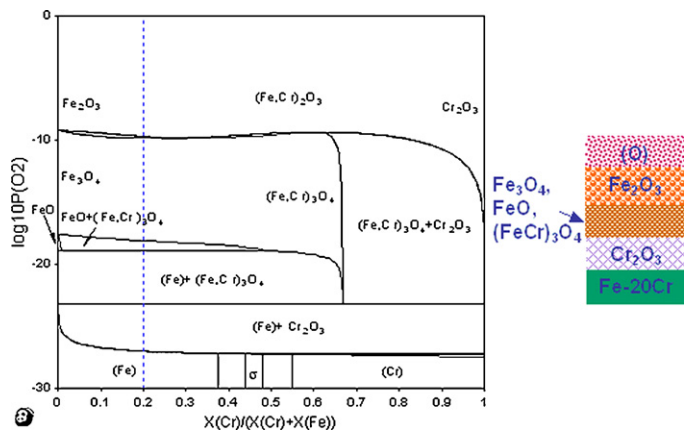

Fig. 3. Calculated stability diagram (also called predominance diagram, or chemical potential diagram) of Fe–Cr–O at 800 °C. The blue dashed line indicates the Fe–20Cr alloy composition. *X* indicates atomic fraction.
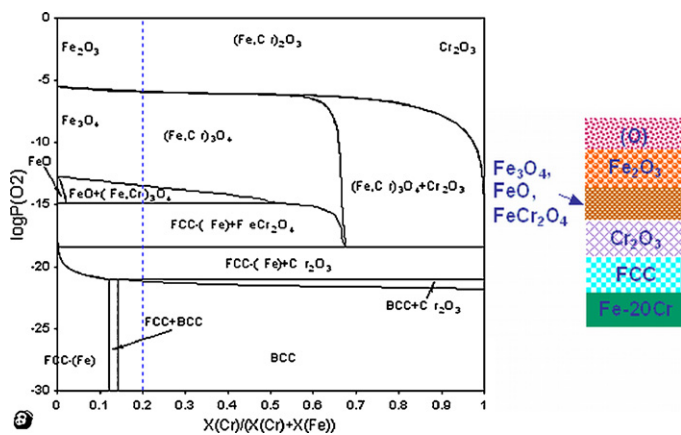
Fig. 4. Calculated stability diagram (also called predominance diagram, or chemical potential diagram) of Fe–Cr–O at 1000 °C. Note that the blue dashed line indicates the Fe–20Cr alloy composition.

may present, including Spinel, Halite, and Corundum-Cr_2O_3. At low oxygen partial pressures, BCC and the σ phase are in equilibrium with Cr-rich $(Cr,Fe)_2O_3$ Corundum phase. For Fe–20Cr stainless steel, sequence of oxide formation is illustrated by the schematic diagram. It indicates that at the oxide/metal interface (low PO_2 region) Cr_2O_3 is anticipated to form in contact with the metallic stainless steel. At the oxide surface, the phase stability diagram predicts Fe_2O_3. In between these two layers, several oxides may form, i.e. Fe_3O_4, FeO, $FeCr_2O_4$-Spinel. When compared to experimental observations, thermodynamic calculations are in agreement with oxide phases that are found in the oxidized stainless steels. Detailed experimental observations and thermodynamic calculations are discussed later.

Fig. 4 shows the calculated stability diagram at 1000 °C. It has a similar trend to that at 800 °C. However, there are two main differences. First, at the oxide/metal interface, FCC-(Fe) may form instead of the σ phase as in the 800 °C case. The implication of the existence of the FCC phase is that the diffusion kinetics may be altered. Second, each phase equilibrium window shifts toward higher PO_2. As in the figure for 800 °C, the oxide formation sequence is represented by the schematic diagram.

3.3. Oxidation behavior of ferritic steels as a function of temperatures

The oxidation behavior of GE-13L and AL-441HP were measured by changes in weight and oxide thickness as a function of temperature and time. Weight changes of the steels were normalized to the original area and are summarized in Fig. 5. All samples gained weight throughout the test indicating oxygen ingress and the formation of oxides. For GE-13L, iron–chromium oxides are the primary oxide. For AL-441HP, weight gain was not only a result of faster oxide growth rate the formation of iron–chromium and iron–chromium–manganese Spinel oxides, but also a result of the internal oxidation of titanium.

Initial weight gain of both GE-13L and AL-441HP was high followed by lower weight change rate as protective oxide scale formed. However, rate of change for AL-441HP was higher than that of GE-13L. In other word, AL-441HP continued to gain weight at a faster rate than GE-13L did. Moreover, the total weight gain of AL-441HP was in an order of magnitude greater than that of GE-13L (depending on the temperature). Higher weight gain of AL-441HP was a result of both faster oxidation kinetics (as shown by thicker oxide scale) and internal oxidation of TiO_2.

In order to determine the phases formed during oxidation, the surfaces of the oxidized samples were characterized by X-Ray
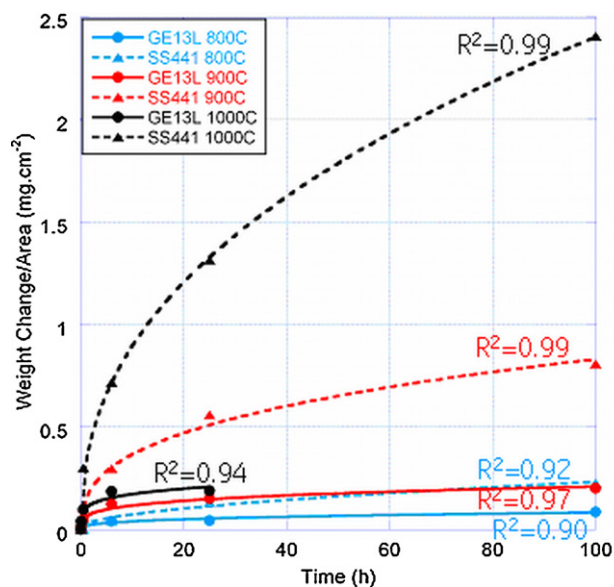

Fig. 5. Comparison of weight change as a function of time and temperature for GE-13L (circles) and AL-441HP (triangles). The parabolic fits are shown in the graph with solid lines (for GE13L) and dashed lines (for AL-441HP). R^2 values indicating the fit of data are shown along with each parabolic fit.

diffraction. Three phases were detected on oxidized GE-13L: Corundum chromium–iron oxide $[(Cr,Fe)_2O_3]$, Spinel chromium–iron oxide $[(Cr,Fe)_3O_4]$, and iron [Fe]. The detection of base metal, Fe, indicates that the oxide scale was thin (<25 μm), allowing the X-ray interaction volume to penetrate through the oxide layer and sample the bulk alloy. For AL-441HP, XRD of the oxidized samples revealed all three phases detected in oxidized GE-13L. However, an additional oxide of rutile (TiO_2) was also detected. Another main difference between GE-13L and AL-441HP was the peak height ratio of Corundum/Spinel as shown in Table 2. The Corundum/Spinel peak ratio in both alloys decreased with time and temperature suggesting higher volume fraction of Spinel $(Cr,Fe,Mn)_3O_4$ in the oxide scale. When compared between alloys, GE-13L showed higher Corundum/Spinel peak height ratio which indicated higher volume fraction of Corundum $(Cr,Fe)_2O_3$ in GE-13L

Experimental results indicate the solubility of iron and chromium in both Corundum-Cr_2O_3 (hematite-type crystal structure) and Spinel-$(Fe,Cr,Mn)_3O_4$ phase (magnetite-type crystal structure), in good agreement with thermodynamic calculations.

Table 2
Relative peak height ratio of Corundum $(Cr,Fe)_2O_3$ and Spinel $(Fe,Cr,Mn)_3O_4$ in GE-13L and AL-441HP after oxidation at 800, 900, and 1000 °C. Phases were identified by X-ray diffraction (XRD).

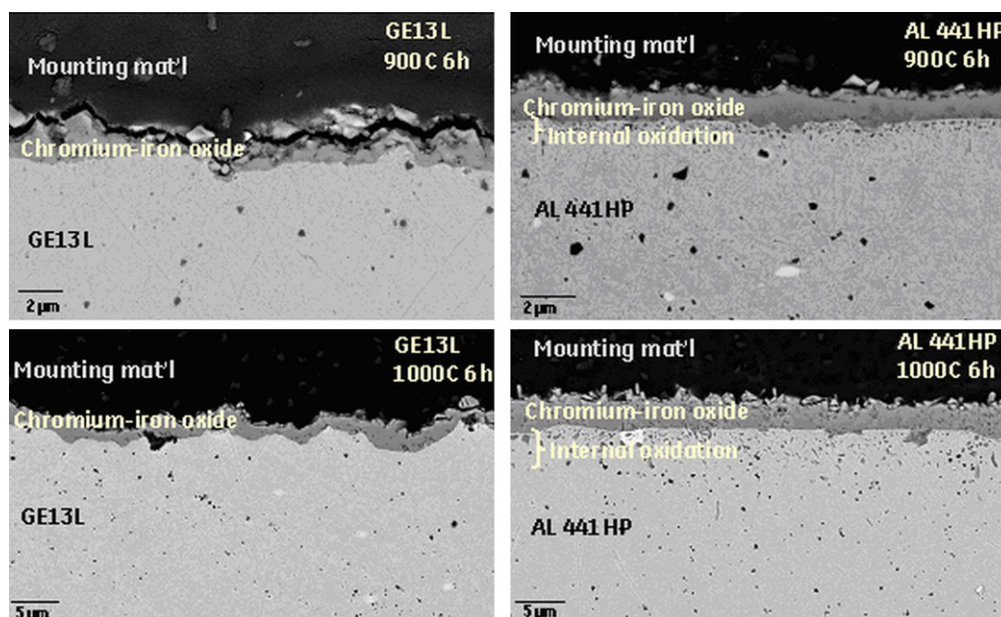| Temperature	Testing time	Alloys	Corundum/Spinel peak height ratio
800 °C	25 h	GE-13L	1.0
		AL-441HP	1.0
	100 h	GE-13L	1.0
		AL-441HP	0.6
900 °C	6 h	GE-13L	1.0
		AL-441HP	0.8
	25 h	GE-13L	1.0
		AL-441HP	0.7
	100 h	GE-13L	0.9
		AL-441HP	0.3
1000 °C	6 h	GE-13L	0.9
		AL-441HP	0.5
	25 h	GE-13L	0.9
		AL-441HP	0.1

Fig. 6. Comparison of oxide thickness as a function of temperature and alloys, GE-13L vs. AL-441HP.

The main difference between the experimental observations and the thermodynamic calculations relates to the outer oxide layer. The stability diagrams at both 800 °C (Fig. 3) and 1000 °C (Fig. 4) indicate that, as a function of oxygen partial pressure, Fe_2O_3 oxide should form as the outer layer, followed by Spinel-$(Fe,Cr,Mn)_3O_4$ while Cr_2O_3 oxide forms as a sublayer at the oxide/metal interface for both GE-13L and AL-441HP. However, experimental data showed only iron–chromium oxide scales of Corundum Cr_2O_3- and Spinel $(Fe,Cr,Mn)_2O_3$-type. The discrepancy could be due to the kinetics of the oxide formation involving the diffusion of each species, the time required for reactions to equilibrate, the difference of partial pressure of oxygen, or the loss of the outer oxide layer during sample mount preparation. Despite the discrepancy, the trend of oxide formation (iron–chromium oxide scale) was self-consistent.

After surface analysis by XRD, further characterization was performed by examining cross sectional samples using an SEM equipped with EDS. Back scattered electron images of selected cross-sectioned oxidized samples are shown in Fig. 6. Oxide thicknesses were measured directly from cross sections of oxidized alloys and are summarized in Table 3. Oxide thickness data correlates well with weight change data and no spallation was observed at all testing temperatures through test durations.

Back-scattered electron images of cross section of oxidized GE-13L showed a thin and dense iron–chromium oxide layer. Scratches evident in the cross section images are due to metallographic effects (sectioning and polishing of the specimens). Energy dispersive spectroscopy (EDS) was used to detect elements present within different layers. The EDS analyses revealed that the oxide layer consisted primarily of chromium and oxygen. A small peak of Fe was also detected potentially indicating the solubility of Fe in chromium oxide or possibly Fe–Cr Spinel. Both phases are thermodynamically stable as indicated earlier in thermodynamic model. Moreover, due to the thin oxide scale, the interaction volume of the electron beam could sample Fe from base alloy.

For AL-441HP, the oxide scale of the 800 °C sample was dense and thin (1.1 μm after 100 h at 800 °C). Oxide scales at 900 and 1000 °C were dense similar to that of GE-13L. EDS analysis of oxide scale indicated that the oxide layer consisted mostly of chromium and oxygen with a small amount of iron. Internal oxidation primarily consisted of TiO_2 was observed in 900 °C and 1000 °C samples. The depth of internal oxidation increased with increasing temperature. AL-441HP contains between 0.1 and 0.6 wt% Ti and internal oxidation of a stainless steel containing titanium was also observed by Huczkowski et al. [19]. Internal oxidation of TiO_2 contributed, in part, to higher weight gain observed in AL-441HP (compared to GE-13L).

4. Discussion

4.1. Kinetic analysis at 800 °C, 900 °C, and 1000 °C

The rate of weight change as a function of temperature is significantly greater for AL-441HP when compared to GE-13L at 800 °C, 900 °C, and 1000 °C. Both the internal oxidation and the lower chromium content in AL-441HP likely contribute to the higher weight gain as well as the higher rate of change due to higher volume fraction of Spinel-$(Cr,Fe)_3O_4$ (Table 2) non-protective iron-rich

Table 3
Oxide thickness of GE-13L and AL-441HP oxidized at 800, 900, and 1000 °C.

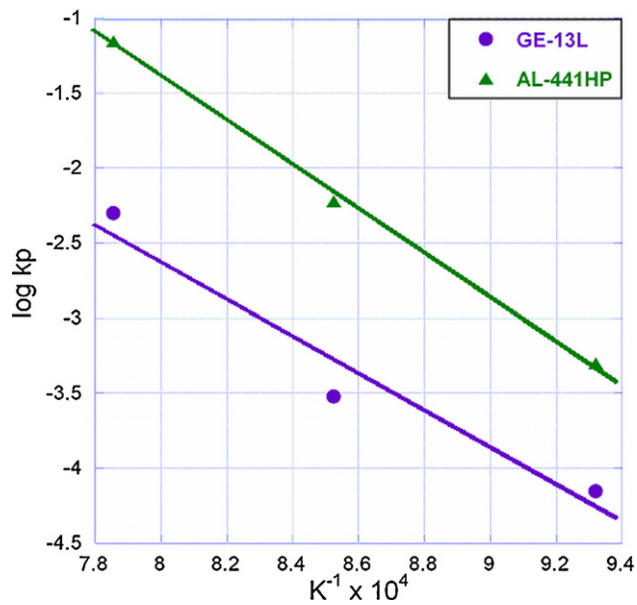| Testing time	Oxide thickness (μm)					
	800 °C		900 °C		1000 °C	
	GE-13L	AL-441HP	GE-13L	AL-441HP	GE-13L	AL-441HP
6 h	Nil	Nil	0.7	1.4	1.2	3.9
25 h	0.2	0.8	1.1	1.8	3.1	8.3
100 h	0.5	1.1	1.7	3.5	8.6	13.1

Fig. 7. The oxidation rate constant as a function of inverse temperature of GE-13L and AL-441HP oxidized at 800–1000 °C.

oxide scale. No internal oxidation was observed in GE-13L at any test temperature.

The oxidation behaviors of GE-13L and AL-441HP follow the parabolic rate law. The oxidation kinetics were assessed based on weight change data and are shown in the Arrhenius plot in Fig. 7. Parabolic constants of both GE-13L and AL-441HP increase with temperature indicating enhanced kinetics at higher temperature.

The parabolic rate constants of AL-441HP are an order of magnitude greater than that of GE-13L at all temperatures. As such, oxide scales on AL-441HP are consistently thicker than that on GE-13L at similar times and temperatures (Fig. 6). The faster kinetics of AL-441HP oxidation is likely a combined result of internal oxidation and lower chromium content. The effect of the chromium content will be discussed in the next section (Section 4.2) by combining the experimental results with thermodynamic calculations.

The oxidation behavior of AL-441HP is more complex than GE-13L due to impurities/alloying elements present in AL-441HP. Although a chromium oxide former, AL-441HP contains titanium as well as silicon, both of which are oxide formers. Internal oxidation of AL-441HP was evident in this oxidation study as indicated in XRD and cross section results (Fig. 6). The formation of silica was not detected by the methods used in the examination of oxidized AL-441HP. However, the test duration may not be sufficient for silica scale to form. Jablonski et al. [20] reported the formation of silica in samples oxidized at 800 °C for 2000 h by TEM. Therefore, further testing and more detailed characterization should be done to ensure the absence of continuous silica scale under long term operation.

4.2. Effects of chromium concentrations

Chromium content is expected to be a primary factor in the formation of chromium oxide scale in ferritic stainless steels. In this study, AL-441HP with 18 wt% Cr is compared to GE-13L which has 20 wt% Cr. In order to investigate effects of chromium content in this range, thermodynamic calculations were performed and compared with experimental data.

Fig. 8(a) and (b) shows the calculated phase fractions for the Corundum and Spinel phases as a function of PO_2 in log scale for Fe–20Cr and Fe–18Cr alloys at 900 °C and 1000 °C, respectively. For both alloys, with increasing Cr content, the relative fraction of Cr-
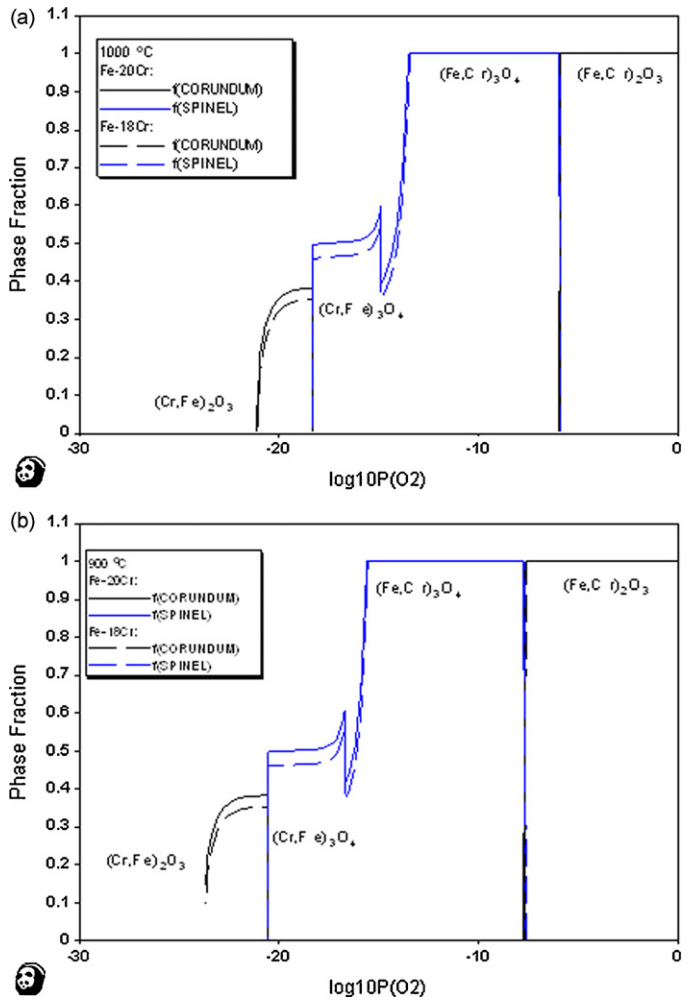

Fig. 8. Calculated the fraction of Corundum and Spinel phases as a function of PO_2 in two alloys: Fe–20Cr and Fe–18Cr: (a) 900 °C and (b) 1000 °C.

rich Spinel $((Cr,Fe)_3O_4)$ and Cr-rich Corundum (Cr_2O_3) increases. However, the volume fraction of the Fe-rich Corundum (Fe_2O_3) and the Fe-rich Spinel $((Fe,Cr)_3O_4)$ is independent of the Cr content. Furthermore, as shown in Table 4, the calculations also indicate that for both temperatures (900 and 1000 °C), the Fe–20Cr tends to have a slightly higher ratio of Corundum to Spinel content than the Fe–18Cr. The trend of higher Corundum/Spinel ratio was also observed in the oxidation experiment (Table 2).

Thermodynamic calculations suggest that higher chromium content results in an oxide with a higher fraction of Corundum $((Cr,Fe)_2O_3)$ compared to the Spinel $((Fe,Cr)_3O_4)$ phase. This result is consistent with the experimental results (Table 2). At 900 °C, the oxide scale of GE-13L (20 wt% Cr) appears to have a higher weight fraction of Corundum phase (Table 2) than AL-441HP. At all testing conditions (temperature & time), the relative ratio of Corundum/Spinel phase in GE-13L is higher than in AL-441HP (Table 2). It should be pointed out that Mn which is present in AL-441HP but

Table 4
Calculated ratio between the fraction of Corundum and that of Spinel phase at a specific PO_2 where these two phases are in equilibrium.

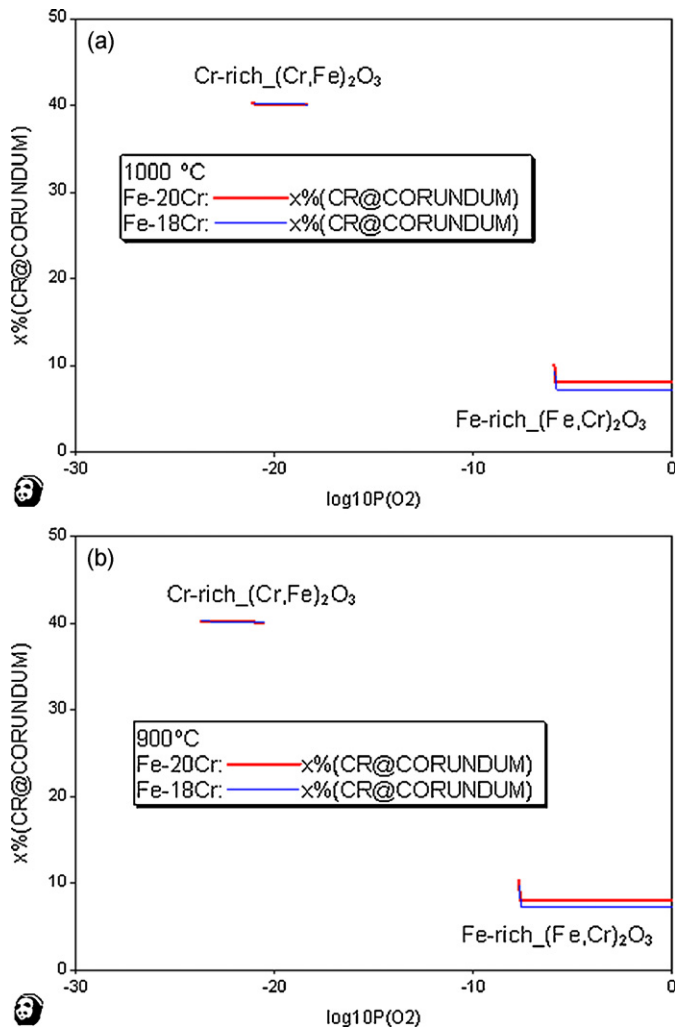| Condition	Phase amount ratio: Corundum/Spinel	
	Fe–20Cr	Fe–18Cr
900 °C (log PO_2 = −20.58)	0.771	0.767
1000 °C (log PO_2 = −18.37)	0.774	0.770

Fig. 9. Calculated Cr-content in the Corundum phase as a function of P_{O2} in log scale for Fe–20Cr and Fe–18Cr alloys, (a) 900 °C and (b) 1000 °C.

not in GE-13L is a Spinel-phase stabilizer. Hence, the presence of Mn could decrease the Corundum/Spinel ratio in AL-441HP.

Since Cr and Fe are miscible in both the Corundum and Spinel phases, the difference in chromium concentration may affect not only the fraction of oxides formed, but also the ratio of Cr/Fe in each phase. Fig. 9 shows the calculated Cr-content in the Corundum phase as a function of PO_2 in log scale for Fe–20Cr and Fe–18Cr alloys at (a) 900 °C and (b) 1000 °C. For both temperatures, the calculations show that in the Fe-rich Corundum phase, the Cr-content appears to follow the same trend as the overall Cr content in the alloy. In other words, the Fe-rich Corundum phase $(Fe,Cr)_2O_3$ in Fe–20Cr has slightly higher Cr-content than that of Fe–18Cr. However, the Cr-content in the Cr-rich Corundum phase $(Cr,Fe)_2O_3$ seems to be insensitive to the overall Cr concentration in the alloy.

As previously shown in Fig. 6 when the oxidation behaviors of the two steels are compared under identical conditions, it is clear that the oxide scale of GE-13L is thinner than that of AL-441HP, suggesting a more protective oxide scale. Kubaschewski and Hopkins [9] proposed that in chromia-forming steels, oxides with higher chromium concentration in the Corundum and Spinel phases are more desirable due to increased protectiveness. However, this interpretation takes into account only the chromium content and not the effects of other alloying elements. In AL-441HP, other alloying elements such as Ti form oxides that affect the weight change of the oxidized samples. Gertsricken and Dekhtyar [26] investigated
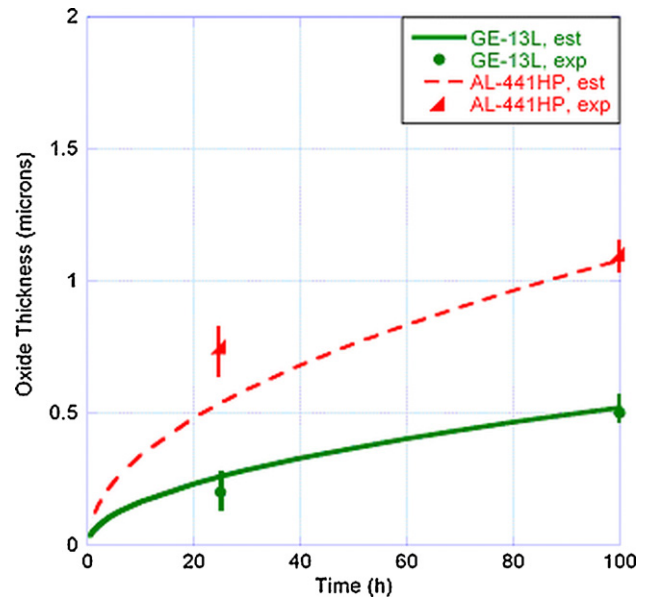

Fig. 10. Comparison of oxide thicknesses between calculated (est, solid and dash lines) and experimental results (exp, circle and triangle symbols) of GE-13L and AL-441HP oxidized at 800 °C.

the effects of alloying elements on the diffusion rate of chromium in iron at 950–1050 °C. They indicated that Ti, Si, and Nb decrease chromium diffusion rate in iron by a half to one order of magnitude [26]. The Ti, Si, and Nb presented in AL-441HP (but not in GE-13L) may lower the kinetic rate of chromium oxide formation, and thus have a detrimental effect on the formation of a protective oxide scale. Moreover, the presence of several alloying elements not only individually influence the diffusion rates of Cr and Fe, but may also have interaction effects on the overall oxidation behavior of the stainless steel.

For steels with higher chromium contents, thermodynamic calculations suggest increased Corundum/Spinel ratios, which is in good agreement with experimental results. Alloys with higher Cr content also form oxides with higher Cr/Fe ratio in each phase. GE-13L (20 wt% Cr) shows better oxidation resistance over AL-441HP (18 wt% Cr) from experimental results.

4.3. Oxide thickness analysis

A kinetic analysis of GE-13L and AL-441HP reveals that the oxidation of both alloys follows the parabolic rate law. The difference between the parabolic constants of GE-13L and AL-441HP is substantial with parabolic constants of AL-441HP an order of magnitude greater than that of GE-13L (Fig. 7). This difference is also evident in higher weight gain and thicker oxides present for AL-441HP oxidized at 800–1000 °C. The higher parabolic constant in AL-441HP was determined from weight change data (Fig. 5). High weight change was a result of faster kinetics as well as the formation of TiO_2 by internal oxidation in AL-441HP (Fig. 6). AL-441HP could contain up to 0.5 wt% of Ti with a typical concentration of 0.2 wt% [18]. Given the amount of Ti in the alloy and the internal oxidation depth, it is estimated that the formation of TiO_2 could contribute 1.3 mg cm^{-2} to weight gain at 1000 °C for 6 h (assuming all Ti oxidized).

According to Wagner's theory of oxidation [29,30], oxide thickness of scale dominated by diffusion follows parabolic rate law as shown in Eq. (5). Fig. 10 reports calculated results at 800 °C along with experimentally measured oxide thickness data for comparison. The calculated and experimental data for GE-13L are within ±5%. For AL-441HP, the discrepancy is in the order of +/− from 0

to 30% and may result from the transition in oxidation behavior from logarithmic to parabolic at the early stages of oxidation. In addition, the error associated with measuring thin oxide scales and small weight change is compounded by the assumptions implicit in the calculations. As exposure time increases, the discrepancy decreases. For AL-441HP, the discrepancy is also affected by internal oxidation, by a variation in oxide thickness and weight change measurements.

Parabolic law [29]:

$$\xi = \sqrt{\frac{k_p t}{(\chi \rho)^2}} \qquad (5)$$

where ξ is the oxide thickness, k_p is a parabolic rate constant in weight, t is the time, χ is the weight fraction of oxygen in the oxide (for example, Cr_2O_3, χ is 48/152), and ρ is the density.

5. Summary

This study contributes to the understanding of the oxidation behavior of ferritic stainless steels for SOFC applications. A combination of thermodynamic modeling and oxidation experiments provides a unique perspective on the understanding of the oxidation behavior of ferritic stainless steels.

A self-consistent thermodynamic description (database) of Fe–Cr–O ternary system focusing on the SOFC operation temperatures 800–1000 °C was obtained and several observations applicable to ferritic stainless steels are found. First, on the alloy side, FCC-Fe may form at 900 and 1000 °C, with potential implications on the kinetics of oxide scale growth. Second, phase equilibria at high temperature (1000 °C) shift toward higher PO_2 region. Furthermore, the amount and composition of the oxide phases as a function of PO_2 were calculated based on the assumption that phase equilibrium prevails in the oxidation process (which may not be the case). Results from the thermodynamic models were compared with experimental data and found to be in good agreement.

It was also found that the alloy Cr content will not have significant effect on the oxide formation but does have an appreciable influence on the relative fraction of some of the oxide phases. Combining isothermal sections and the stability diagrams, a possible phase forming sequence was deduced for the oxidation process of the SOFC cathode interconnect stainless steel alloy. The effect of chromium content is evaluated in terms of the volume fraction of two different oxides: Corundum-$(Fe,Cr)_2O_3$ and Spinel-$(Fe,Cr)_3O_4$. It is found that steel with higher chromium content (GE-13L) showed higher Corundum/Spinel fraction ratio. Furthermore, alloy with higher Cr content appears to result in Fe-rich Corundum phase $(Fe,Cr)_2O_3$ with higher Cr content. These results lead to a more protective oxide scale in alloy with higher Cr content.

The kinetic evaluation of the thermally grown oxide on GE-13L (20 wt% Cr) and AL-441HP (18 wt% Cr) was performed and found to follow the parabolic rate law over the temperatures of interest (800–1000 °C). The parabolic constants of AL-441HP were an order of magnitude higher than that of GE-13L at all temperature indicating faster kinetics in AL-441HP. Further investigation of oxide morphology revealed the formation of thicker oxide scale in AL-

441HP than that in GE-13L. Moreover, internal oxidation of TiO_2 in AL-441HP was observed whereas no evidence of internal oxidation was observed in GE-13L.

An oxide thickness prediction model was constructed for GE-13L and AL-441HP in the temperature ranges 800–1000 °C. The predicted results are in good agreement with experimental data.

Future work includes a more detailed study on the implications of accelerated oxidation testing though increased temperature to better understand the potential impact of the FCC phase.

References

[1] S.P. Jiang, J.P. Zhang, L. Apateanu, K. Foger, J. Electrochem. Soc. 147 (2000) 4013.
[2] P.K. Srivastava, T. Quach, Y.Y. Duan, R. Donelson, S.P. Jiang, F.T. Ciacchi, S.P.S. Badwal, Solid State Ionics 99 (1997) 311.
[3] E. Ivers-Tiffee, W. Wersing, M. Schiebl, H. Greiner, Ber. Bunsen-Ges. Phys. Chem. 94 (1990) 978.
[4] W.J. Quadakkers, J.P. Abellan, V. Shemet, L. Singheiser, Mater. High Temp. 20 (2) (2003) 115–127.
[5] P. Jian, L. Jian, H. Bing, G. Xie, J. Power Sources 158 (2006) 354–360.
[6] Z. Yang, G. Xia, P. Singh, J.W. Stevenson, Solid State Ionics 176 (2005) 1495–1503.
[7] A.M. Huntz, A. Reckmann, C. Haut, C. Severac, M. Herbst, F.C.T. Resende, A.C.S. Sabioni, Mater. Sci. Eng. A 447 (2007) 266–276.
[8] A.N. Hansson, M.A.J. Somers, Mater. High Temp. 22 (3–4) (2005) 223–229.
[9] O. Kubaschewski, B.E. Hopkins, Oxidation of Metals and Alloys, Butterworths Scientific Publications, 1953.
[10] S.C. Singhal, Solid State Ionics 152–153 (2002) 405.
[15] L. Kjellqvist, M. Selleby, B. Sundman, CALPHAD 32 (2008) 577.
[16] M. Hillert, J. Alloys. Compd. 320 (2001) 161.
[17] G. Inden, Z. Metallkd. 66 (1975) 577.
[18] Technical Data for Stainless Steel AL-441HP™ Alloy, ATI Allegheny Ludlum.
[19] P. Huczkowski, N. Christiansen, V. Shemet, L. Niewolak, J. Piron-Abellan, L. Singheiser, W.J. Quadakkers, Fuel Cells 6 (2) (2006) 93–99.
[20] P.D. Jablonski, C.J. Cowen, J.S. Sears, J. Power Sources 195 (3) (2010) 813–820.
[21] M. Hillert, M. Jarl, CALPHAD 2 (1978) 227.
[22] Pandat—Phase Diagram Calculation Software Package for Multicomponent Systems, CompuTherm, LLC, Madison, WI 53719, 2008.
[24] C. Wagner, Corrosion Science, 1933.
[26] S. Gertsricken, I.Ya. Dekhtyar, J. Tech. Phys. 20 (1950) 1005.
[29] C. Wagner, Atom Movements, American Society of Metals, Cleveland, OH, 1951.
[30] K. Hauffe, Oxidation of Metals, Plenum Press, New York, 1965.